

Flight Implementation of Shortest-Time Maneuvers for Imaging Satellites

Mark Karpenko*

*Naval Postgraduate School, Monterey, California 93943*Sagar Bhatt[†] and Nazareth Bedrossian[†]*Charles Stark Draper Laboratory, Inc., Houston, Texas 77058*

and

I. Michael Ross[‡]*Naval Postgraduate School, Monterey, California 93943*

DOI: 10.2514/1.62867

Shortest-time maneuvers are constrained time-optimal slews that enable spacecraft to be maneuvered more quickly than conventional rotations. Shortest-time maneuvers can increase a spacecraft's imaging capability without any changes to the hardware. Previous studies have shown that, depending upon the spacecraft design, the increased capability can be over 50%. Motivated by such high increases in efficiencies, the first flight demonstration of a shortest-time maneuver was performed on 10 August 2010 onboard NASA's TRACE Space Telescope. To transition this new technology from flight demonstration to standard operational procedures, several qualification thresholds need to be met. This paper demonstrates two of these qualification thresholds: 1) the ability to consistently and reliably generate flight-implementable shortest-time maneuvers on demand, and 2) flight demonstrations over multiple operational scenarios involving minimum-time slewing, attitude hold for point data collection, and transition maneuvers for scanning operations. The key technology for meeting both thresholds is flight-implementable pseudospectral controls. Flight and operational considerations quickly narrow down the plethora of pseudospectral options to the Legendre and Chebyshev techniques. All flight implementations were performed using the spectral algorithm of the Legendre pseudospectral method.

I. Introduction

IMAGING satellites acquire photographs and other specialized images of specific areas of interest using their onboard sensors. Because each acquired image generates scientific data and/or revenue, there has been great interest in developing algorithms for planning image acquisition sequences in order to maximize the science return and profitability of imaging satellites (for example, see [1,2] and the references therein). A significant factor that influences the outcome of the planning process is the amount of time that is needed to slew the spacecraft between the possible image collection regions. The ability to transition between each imaging region as quickly as possible is important because each region of interest is only in the field of view of the imagining sensor for a limited time. Moreover, reducing the overall slew time increases the number of images that can be acquired during a given window.

Because slew time has a direct influence on the productivity of imaging satellites and other scientific missions, time-optimal attitude maneuvers have been extensively studied. The paper by Scrivener and Thompson [3] surveys the state of the art up to 1994. The main discovery arising from this body of research is the fact that conventional eigenaxis rotations are not time optimal. Although an eigenaxis rotation gives the shortest angular path between two orientations, restricting the motion of the spacecraft about the eigenaxis can severely limit the achievable vehicle acceleration and

rate. Time-optimal attitude maneuvers, on the other hand, provide a choreography of synchronous rotations about all three axes of the body-fixed frame. By rotating about all axes simultaneously, the spacecraft acceleration and rotation rate can, in many cases, be increased far beyond its eigenaxis limits. This allows the spacecraft to be reoriented more quickly than by following the eigenaxis path. The first maneuver performed on orbit to demonstrate the preceding points was implemented on the NASA Transition Region and Coronal Explorer (TRACE) on 10 August 2010 [4].

There are a number of reasons for the relatively large time constant in moving from an initial concept to a successful flight (nearly two decades from the early 1990s to 2010). The early results [5] were largely academic in nature and were limited to kinematic motion planning. More important, however, the performance improvements were not significant enough to warrant a flight demonstration. Typical results showed that the slew time improvement was less than 1% for a 30 deg maneuver [5]. To extract higher performance, it is necessary to exploit the full dynamics of the spacecraft. The first step in this direction is to solve the shortest-time maneuver (STM) problem for nonsymmetric rigid bodies because, from a practical point of view, spacecraft are generally not symmetric. To this end, Shen and Tsiotras [6] first studied the case of an axisymmetric rigid body in 1999. Their work illustrated the overall difficulty of the problem despite the apparent simplicity provided by the axisymmetry. It can be argued that most of their difficulties were centered around the then-absence of a reliable computation technique to solve optimal control problems. This barrier was overcome in 2001 by Proulx and Ross [7] who employed the then newly developed pseudospectral (PS) technique implemented in DIDO [8] to solve the more difficult problem of nonsymmetric rigid bodies. Following this, Fleming [9] and Fleming et al. [10–13] advanced the analysis over several years from 2004 to 2010 to the more realistic cases of spacecraft equipped with various actuators, from magnetic torquers to reaction wheels and control moment gyros (CMGs). These extensive studies were made possible by parallel advances in the robustness of the spectral algorithm [14,15] that were built largely upon the convergence theorems developed by Kang et al. [16–18]. Fleming's results, in particular, advanced the case for flight

Received 19 April 2013; revision received 5 September 2013; accepted for publication 6 September 2013; published online 21 March 2014. Copyright © 2013 by Mark Karpenko, Sagar Bhatt, Nazareth Bedrossian, and I. Michael Ross. Published by the American Institute of Aeronautics and Astronautics, Inc., with permission. Copies of this paper may be made for personal or internal use, on condition that the copier pay the \$10.00 per-copy fee to the Copyright Clearance Center, Inc., 222 Rosewood Drive, Danvers, MA 01923; include the code 1533-3884/14 and \$10.00 in correspondence with the CCC.

*Research Assistant Professor, Department of Mechanical and Aerospace Engineering; mkarpenk@nps.edu (Corresponding Author).

[†]Vehicle Dynamics and Control Group.

[‡]Professor and Program Director, Control and Optimization, Department of Mechanical and Aerospace Engineering.

implementation by showing that improvements greater than 50% were possible in comparison with conventional maneuvers. Finally, ground tests were conducted at the Naval Postgraduate School [19] to alleviate flight risks, thereby paving the way for the first flight demonstration of the ideas on the TRACE spacecraft in 2010.

To transition the success of the first flight toward operational use, several additional qualification thresholds need to be met. Among these thresholds is the ability to demonstrate on-demand, consistent, and reliable generation of flight-implementable STMs and, more important, the ability to demonstrate this capability over multiple operational scenarios involving minimum-time slewing, attitude hold for point data collection, and transition maneuvers for scanning operations. Whereas the flight results presented in [4] are sufficient to demonstrate that an STM can indeed be implemented on a real world system, it is impossible to generalize how slew performance can be improved over a larger region of operation from a single maneuver. To address this point, this paper presents the development and successful flight demonstration of several new slew designs that enable performance to be judged over a wider envelope of operation and also meet the qualification thresholds for operational use. The results of this paper are, therefore, important for transitioning this technology toward an operational implementation of the concept. In one of the operationally relevant flight tests, a STAR pattern design [20] is used to demonstrate a collection of STMs that minimize the time to slew through an imaging sequence. This design illustrates how the implementation of the optimal maneuvers can be used to improve data collection throughput within a given imaging window. A second SCAN design [21] presents scanning operations to show how STMs can be used to more efficiently transition the spacecraft between point collection and scanning tasks. Each of the flight tests is developed specifically to stress the spacecraft by demanding operation over a wider range than a single maneuver can provide.

To perform these operationally relevant flight demonstrations, a collection of complex multipoint optimal control problems [15,22,23] had to be solved quickly and reliably. The operational variables in the multipoint optimal control problem are arbitrary boundary conditions, which are demanded by the operational environment. The problem formulation is further complicated by the need to include a nonlinear model of the relevant spacecraft dynamics as well as other nonlinear state and control constraints on the operation of the system to ensure flight success. One example of such a constraint is the nonlinear reaction wheel torque-momentum envelope that arises due to power and voltage limitations of the spacecraft bus. Each resulting optimal control problem comprises over 19 differential equations with both differential and algebraic constraints. As noted before, such problems cannot be solved reliably and consistently by the so-called indirect methods or by traditional collocation methods. PS techniques, on the other hand, offer the requisite breakthrough for operational use [24]. As pointed out in [24–28], however, not all PS methods are reliable nor convergent. To date, only the Legendre and Chebyshev PS methods have been proven to be convergent for arbitrary boundary conditions, a key necessity for operational use. To ensure flight success, the Legendre PS method was chosen for its proven consistency, reliability, and prior flight experience [29,30]. To drive home this flight critical decision point, we also show in this paper the potential disastrous consequences of choosing a PS method that is not convergent.

II. Spacecraft Description

The TRACE spacecraft (Fig. 1) was part of the NASA SMall EXplorer (SMEX) mission.[§] The scientific mission of the space telescope was to document the fine scale magnetic features of the solar surface as well as features of the transition region and corona. To perform this task, the TRACE attitude control system (ACS) uses reaction wheels to perform small angle slews between the various regions of interest according to a quaternion command timeline stored onboard the spacecraft. The TRACE ACS is capable of maintaining pitch and yaw pointing accuracy of 20 arcseconds [31],



Fig. 1 The TRACE spacecraft undergoing a prelaunch checkout at NASA.

and can also execute large angle reorientation maneuvers using a nonlinear momentum control logic, despite the fact that such maneuvers were not part of the original mission objectives.

A. Spacecraft Equations of Motion

A model of the rotational motion of the TRACE satellite can be constructed by augmenting the rotational dynamic equations with an appropriate representation of the vehicle kinematics, such as the quaternion parameterization. The rotational dynamic equations are derived by considering the angular momentum of the spacecraft and reaction wheel system,

$$\mathbf{H} = I\boldsymbol{\omega} + \sum_{i=1}^n \mathbf{a}_i h_{w,i} \quad (1)$$

where \mathbf{H} is the total angular momentum of the system with respect to the body-fixed frame. Matrix I is the inertia tensor of the spacecraft with freely rotating reaction wheels, and vector $\boldsymbol{\omega}$ is the inertial angular rate of the spacecraft expressed in the body frame. The summation in Eq. (1) is the total angular momentum associated with an array of n reaction wheels. Unit vectors \mathbf{a}_i give the orientation of the spin axis of each reaction wheel with respect to the spacecraft coordinate system. Each product $\mathbf{a}_i h_{w,i}$ therefore represents the transformation of the reaction wheel momentum from the individual actuator frames to the body-fixed frame.

In the absence of any external torques acting on the spacecraft, momentum must be conserved. As a consequence, the time rate of change of the system angular momentum in the inertial frame is null. Thus, by applying the transport theorem [32] to Eq. (1), the following relation is obtained:

$$\frac{d}{dt}(\mathbf{H}) + \boldsymbol{\omega} \times \mathbf{H} = 0 \quad (2)$$

Equation (2) can be expanded and rearranged to give

$$I\dot{\boldsymbol{\omega}} + \sum_{i=1}^n \mathbf{a}_i \dot{h}_{w,i} + \boldsymbol{\omega} \times \left(I\boldsymbol{\omega} + \sum_{i=1}^n \mathbf{a}_i h_{w,i} \right) = 0 \quad (3)$$

The angular momentum of each reaction wheel about its axis of rotation is

$$h_{w,i} = I_{w,i}(\boldsymbol{\Omega}_{w,i} + \mathbf{a}_i^T \boldsymbol{\omega}) \quad (4)$$

[§]Data available at <http://trace.lmsal.com/> [retrieved 22 March 2013].

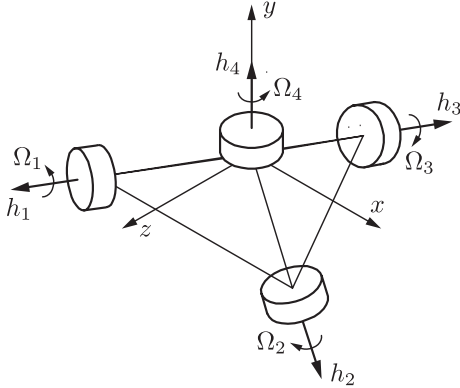


Fig. 2 Orientation of TRACE reaction wheel array.

where $I_{w,i}$ is the inertia of the reaction wheel about its spin axis and $\Omega_{w,i}$ is the angular rate of the reaction wheel relative to the actuator frame. Terms $\mathbf{a}_i^T \boldsymbol{\omega}$ account for the additional angular momentum arising due to the motion of the spacecraft body. The differential equation describing the reaction wheel dynamics is

$$\dot{\Omega}_{w,i} = I_{w,i}^{-1} \tau_{w,i} - \mathbf{a}_i^T \dot{\boldsymbol{\omega}} \quad (5)$$

In Eq. (5), variable $\tau_{w,i}$ refers to the torque provided by reaction wheel i and is defined in the reaction wheel frame.

Substituting Eqs. (4) and (5) into Eq. (3) allows the spacecraft rotational dynamics to be written in the following matrix form:

$$\begin{bmatrix} \dot{\boldsymbol{\omega}} \\ \dot{\Omega}_{w,1} \\ \vdots \\ \dot{\Omega}_{w,n} \end{bmatrix} = \Gamma^{-1} \begin{bmatrix} -\boldsymbol{\omega} \times (I\boldsymbol{\omega} + \sum_{i=1}^n \mathbf{a}_i I_{w,i} \Omega_{w,i} + \mathbf{a}_i I_{w,i} \mathbf{a}_i^T \boldsymbol{\omega}) \\ \tau_{w,1} \\ \vdots \\ \tau_{w,n} \end{bmatrix} \quad (6)$$

where

$$\Gamma = \begin{bmatrix} I + \sum_{i=1}^n \mathbf{a}_i I_{w,i} \mathbf{a}_i^T & \mathbf{a}_1 I_{w,1} & \cdots & \mathbf{a}_n I_{w,n} \\ I_{w,1} \mathbf{a}_1^T & I_{w,1} & \cdots & 0 \\ \vdots & \vdots & \ddots & \vdots \\ I_{w,n} \mathbf{a}_n^T & 0 & \cdots & I_{w,n} \end{bmatrix} \quad (7)$$

To complete the mathematical model of the spacecraft dynamics, the attitude kinematics are modeled using the quaternion differential equation [33]

$$\dot{\mathbf{q}} = \frac{1}{2} Q(\boldsymbol{\omega}) \mathbf{q} \quad (8)$$

where $Q(\boldsymbol{\omega})$ is the skew-symmetric matrix,

$$Q(\boldsymbol{\omega}) = \begin{bmatrix} 0 & \omega_3 & -\omega_2 & \omega_1 \\ -\omega_3 & 0 & \omega_1 & \omega_2 \\ \omega_2 & -\omega_1 & 0 & \omega_3 \\ -\omega_1 & -\omega_2 & -\omega_3 & 0 \end{bmatrix} \quad (9)$$

B. Attitude Control System

The TRACE spacecraft employs four reaction wheels for primary attitude control along with three magnetic torquer coils for momentum management. The reaction wheels are arranged in a tetrahedral array, as shown in Fig. 2. This arrangement gives four-for-three redundancy to ensure that full control capability is retained in the event of a failure of any single wheel [31]. The spacecraft body rates are measured using three dual-axis gyros. Onboard quaternion propagation is carried using the rate gyros in conjunction with measurements from a three-axis fluxgate magnetometer and a Kalman filter.

Reorientation maneuvers are performed in the science point mode using a switching nonlinear momentum control law [31]. A block diagram of the ACS is shown in Fig. 3. Because the ACS was originally designed to implement eigenaxis maneuvers, the first step in the control process is to determine the rotation angle Φ and Euler axis e that zeros the attitude error with respect to the current target quaternion. The control logic then determines an appropriate momentum command from an angular rate schedule that depends on the magnitude of the computed rotation angle. For large angle maneuvers, the rate command is determined based on the square root of the rotation angle error and is software limited in order to avoid saturating the rate gyro measurements. When the attitude error is small, the spacecraft rate command follows a linear control law where the commanded rate is proportional to the desired rotation angle. These operations are captured by the following equation:

$$\omega_{cmd} = \begin{cases} K_P \sqrt{\Phi} & \text{if } \Phi \geq 2.8^\circ \\ K_P \Phi & \text{if } \Phi < 2.8^\circ \end{cases} \quad (10)$$

In Eq. (10), the commanded rate can be limited to a value below the specified rate gyro software limit through adjustment of the proportional gain K_P .

Referring to Fig. 3, the reaction wheel momentum command vector \mathbf{h}_{cmd} is computed by distributing the commanded angular rate along the eigenaxis and accounting for the spacecraft inertia to obtain the commanded momentum in the spacecraft body frame. The momentum command is then transformed to the individual reaction wheel frames by control allocation matrix $\bar{\mathbf{A}}$. The reaction wheel momentum command vector is, therefore,

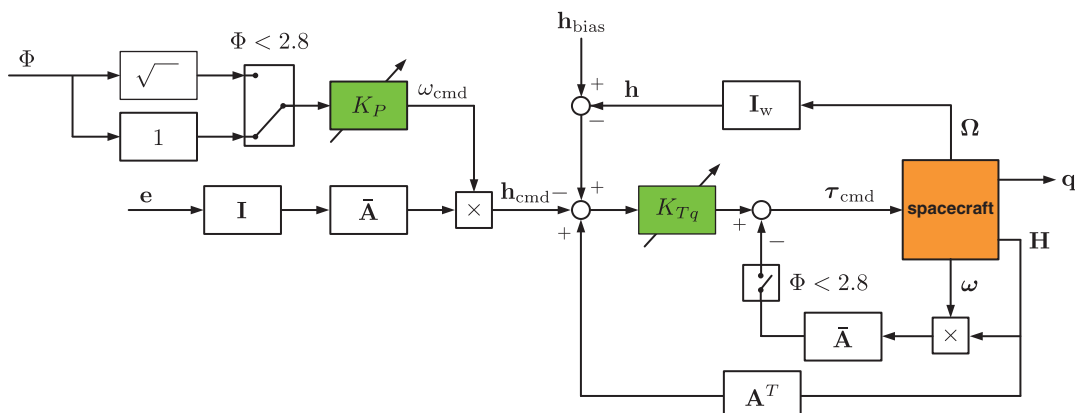


Fig. 3 Block diagram of TRACE attitude control system.

$$\mathbf{h}_{\text{cmd}} = \omega_{\text{cmd}} \bar{A} \mathbf{I} \mathbf{e} \quad (11)$$

The individual reaction wheel torque commands are then computed as

$$\boldsymbol{\tau}_{\text{cmd}} = K_{Tq} (\mathbf{h}_{\text{cmd}} + A^T \mathbf{H} + \mathbf{h}_{\text{bias}} - \bar{A}(\boldsymbol{\omega} \times \mathbf{H})) \quad (12)$$

where parameter K_{Tq} is an adjustable slew torque gain, $\mathbf{H} = I\boldsymbol{\omega} + AI_w\boldsymbol{\Omega}$ is the total system momentum vector expressed in the body-fixed frame, I_w is a diagonal matrix of reaction wheel spin axis inertia values, and $A = [\mathbf{a}_1 | \mathbf{a}_2 | \mathbf{a}_3 | \mathbf{a}_4]$ is the column matrix of unit vectors relating the wheel spin axes to the spacecraft frame. Note that, in Eq. (12), the reaction wheel torque commands are only compensated for gyroscopic terms during large angle slews, when $\Phi \geq 2.8$ deg. In addition, a bias momentum \mathbf{h}_{bias} is maintained for each wheel to ensure that the reaction wheels operate at nonzero nominal rates. This is done to minimize zero-speed crossings, where wheel rate estimation is unreliable and the presence of stiction prevents precise motion control.

Prior to applying the commanded torques to the reaction wheel array, they are filtered in order to suppress the excitation of the flexible modes of the spacecraft structure. Neglecting the fast dynamics of the reaction wheel speed control system, the relationship between the ACS commanded torque $\boldsymbol{\tau}_{\text{cmd}}$ and actual reaction wheel torque demands $\boldsymbol{\tau}_w$ can be written in the following form:

$$\dot{\mathbf{x}}_{\text{filt}} = A\mathbf{x}_{\text{filt}} + B\boldsymbol{\tau}_{\text{cmd}} \quad \boldsymbol{\tau}_w = C\mathbf{x}_{\text{filt}} + D\boldsymbol{\tau}_{\text{cmd}} \quad (13)$$

where \mathbf{x}_{filt} is the vector of filter states and A , B , C , and D are the matrices of torque filter coefficients having the appropriate dimensions. In addition to filtering the commanded torques, the nonlinear constraints on the maximum momentum storage and reaction wheel power limits shown in Fig. 4 must also be enforced by ensuring that, at any point in time, the commanded reaction wheel torques are bounded by the curves $\tau_L(h)$ and $\tau^U(h)$. Relevant attitude control system parameters for the TRACE spacecraft are provided in Zimbelman et al. [31].

C. Conventional Maneuver Implementation

The science point mode of the TRACE attitude control system can be used in two different ways to implement a large angle eigenaxis maneuver. In the first, the desired target quaternion is read from the spacecraft command buffer and an appropriate rate command is generated using the nonlinear square root control law in Eq. (10). Figure 5 shows spacecraft attitude and angular rate commands for a large angle eigenaxis slew along with time histories of the spacecraft response when the maneuver was executed on orbit. Referring to Fig. 5b, the rate command is initially limited by the control logic in order to avoid rate gyro saturation. Once the attitude error has been reduced to a suitable level, the rate command is varied in accordance with the square root relation in Eq. (10) to decelerate the spacecraft. The small discontinuity in the rate command at $t \approx 1.1$ time units

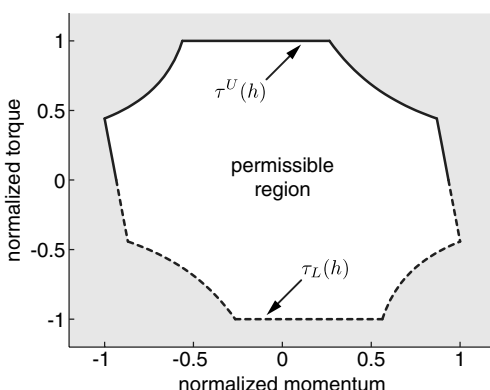


Fig. 4 TRACE reaction wheel torque–momentum envelope.

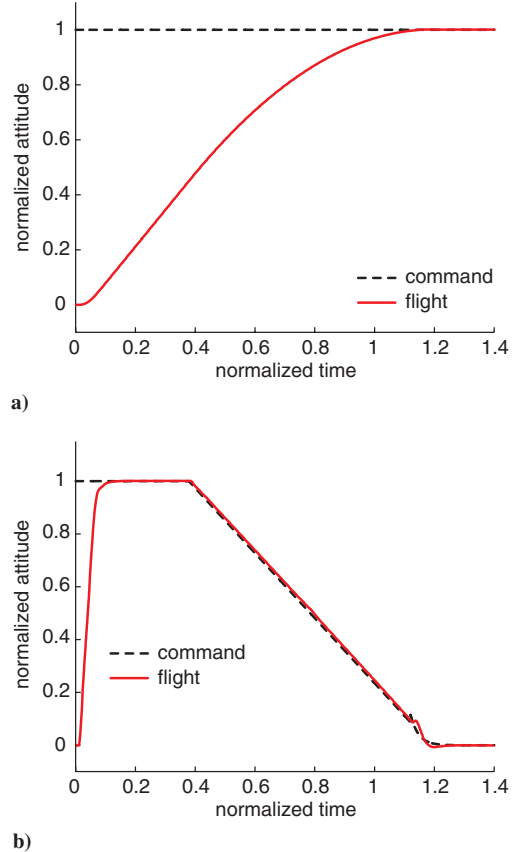


Fig. 5 Eigenaxis slew using nonlinear control law: a) normalized attitude, and b) normalized rate.

occurs when the control logic switches between the square root and proportional rate schedules.

The other approach for implementing large angle eigenaxis maneuvers on the TRACE spacecraft is to operate the ACS using the linear controller only. This mode of operation is enabled by executing an attitude command timeline in such a way that the rotation error is always less than the switching threshold. The spacecraft attitude and angular rate commands for a large angle eigenaxis maneuver performed using the linear controller only are shown in Fig. 6, along with relevant flight results. In contrast to Fig. 5, implementing a large angle slew using only the linear control logic allows the spacecraft angular rate to be maintained at the saturation level throughout the entire maneuver. This type of response is similar to the manner in which slews are performed on imaging satellites. Thus, to facilitate performance comparisons between eigenaxis and minimum-time maneuvering in the context of example imaging operations, the linear control logic was employed in the flight test experiments.

As shown in Fig. 6b, the constant rate command profile used to implement the eigenaxis maneuver causes the body rate to slightly overshoot the software imposed saturation limit. This characteristic of the response results from the fact that the TRACE ACS has no provision for limiting the body rate buildup when the linear proportional control law is used to slew the spacecraft through large angles. Moreover, this aspect of the flight software could not be modified for the flight tests. Because the software gyro saturation limit is smaller than the hard saturation limit of the gyro hardware, however, control of the spacecraft can be properly maintained during the brief overshoot period. On the other hand, if the hard limit were exceeded, the only way to alleviate the problem would be to enforce a more stringent body rate constraint. As will be seen later, overshooting the software gyro saturation limit is not an issue when implementing the designed STMs because the body rate buildup can be properly shaped by the optimal control. This feature of the

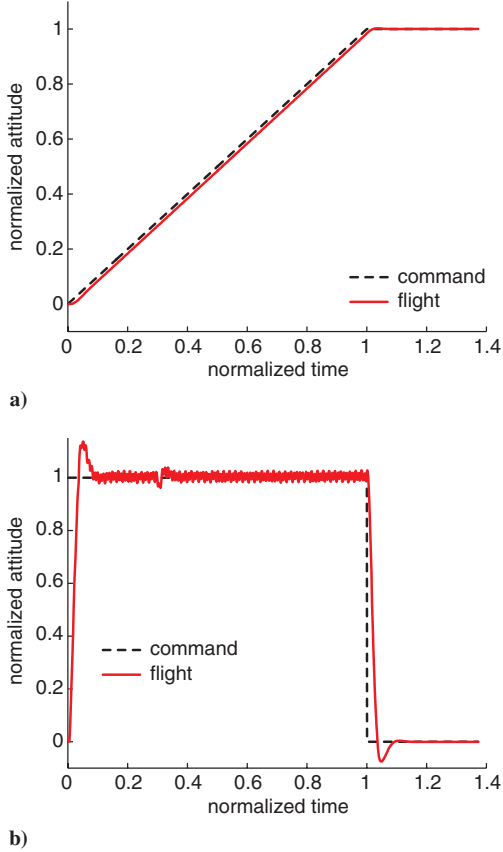


Fig. 6 Eigenaxis slew using linear control law: a) normalized attitude, and b) normalized rate.

maneuver design is accomplished by including the reaction wheel dynamics and associated constraints as part of the optimal control problem.

III. Shortest-Time Maneuver Design and Flight Test

A. Optimal Control Formulation

Based on the models developed in Sec. II, a suitable formulation of each individual problem making up the multipoint operational optimal control problem can be defined as

where the symbol $B(\mathbf{x}_0, \mathbf{x}_f)$ is used to emphasize that the boundary conditions on the problem change between individual maneuvers and that the entire operational problem is a multipoint problem with arbitrary boundary conditions. Note that the formulation of the optimal control problem not only accounts for the spacecraft dynamics but also all of the relevant spacecraft actuator, sensor, and operational constraints. For example, one operational constraint requires that the proper reaction wheel bias momentum be maintained at the beginning and end of each maneuver. This is done by appropriately constraining the initial and final reaction wheel rates.

In Eq. (14), the state space model of the spacecraft dynamics given by Eqs. (6) and (8) is augmented by including the dynamics of the reaction wheel torque command filters in Eq. (13). To ensure that the optimal control solution can actually be implemented on the real spacecraft, the problem formulation also includes constraints on the commandable reaction wheel torque and limits on the reaction wheel momentum. Spacecraft bus power and voltage limits are also incorporated by using the constraint $\tau_L(h) \leq \tau_{w,i}(t) \leq \tau^U(h)$ to ensure that the output torques always remain within the permissible region (Fig. 4). The absolute values of the spacecraft body rates were additionally constrained by setting $\omega_{\max} = 0.5$ deg/s to avoid saturation of the rate gyros.

B. Selecting an Operational Flight-Implementable Method

Obtaining a solution to problem (14) is challenging for a number of reasons, including the high dimensionality of the state space model (19 states and 4 controls), the nonlinear characteristics of the quaternion dynamics, the coupled nature of the dynamical equations, and the need to consider both linear and nonlinear state and control constraints. Furthermore, a purported solution to the problem must be shown to satisfy the necessary conditions of optimality, which assert the existence of covector functions $t \rightarrow (\lambda, \mu, \nu)$ that satisfy certain conditions with respect to the Lagrangian of the Hamiltonian, the endpoint Lagrangian, as well as complementarity conditions on the endpoint and path constraints [34]. The resulting dualized problem is a boundary value problem of 38 differential equations with both differential and algebraic constraints. In addition, a transition to flight implementation requires the near-absolute guarantee of consistent and reliable computation of optimal controls. In particular, for operational implementation, a collection of optimal control problems must be solved for arbitrary boundary conditions that change constantly based on the mission plan.

All of these challenges have been overcome in the past by selecting the Legendre PS method [29,35–37] to solve the underlying optimal control problems. The Legendre PS method was first flight-tested in 2006 when it was used to perform the historic zero-propellant

$$\left. \begin{array}{ll}
 \text{Minimize} & J[\mathbf{x}(\cdot), \mathbf{u}(\cdot), t_f] = t_f \\
 \text{Subject to} & \dot{\mathbf{x}}(t) = \left\{ \begin{array}{l} \mathbf{\Gamma}^{-1} \left[\begin{array}{l} \frac{1}{2} Q(\omega) \mathbf{q} \\ -\omega \times (I\omega + \sum_{i=1}^4 \mathbf{a}_i I_{w,i} \Omega_{w,i}) \\ + \mathbf{a}_i I_{w,i} \mathbf{a}_i^T \omega \\ C \mathbf{x}_{\text{filt}} + D \mathbf{u} \\ A \mathbf{x}_{\text{filt}} + B \mathbf{u} \end{array} \right] \\ \mathbf{u} = \boldsymbol{\tau}_{\text{cmd}} \\ \mathbf{x}_0 = \left[\mathbf{e}_0 \sin\left(\frac{\phi_0}{2}\right), \cos\left(\frac{\phi_0}{2}\right), \omega_0, \Omega_0, \mathbf{x}_{\text{filt},0} \right]^T \\ \mathbf{x}_f = \left[\mathbf{e}_f \sin\left(\frac{\phi_f}{2}\right), \cos\left(\frac{\phi_f}{2}\right), \omega_f, \Omega_f, \mathbf{x}_{\text{filt},f} \right]^T \\ \|\mathbf{q}(t)\| \\ |\omega_i(t)| \leq \omega_{\max}, \quad i = 1, \dots, 3 \\ |\tau_{\text{cmd},i}(t)| \leq \tau_{\text{cmd,max}}, \quad i = 1, \dots, 4 \\ |I_{w,i} \Omega_{w,i}(t)| \leq I_{w,i} \Omega_{\max}, \quad i = 1, \dots, 4 \\ \tau_L(h) \leq \tau_{w,i}(t) \leq \tau^U(h), \quad i = 1, \dots, 4 \end{array} \right\} \\
 B(\mathbf{x}_0, \mathbf{x}_f): & \end{array} \right\} \quad (14)$$

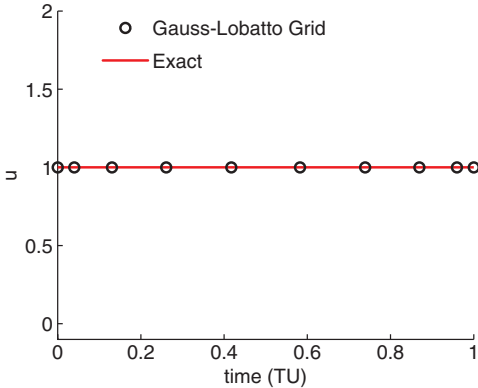


Fig. 7 Illustrating a flight-implementable control solution over a Gauss–Lobatto grid [24].

maneuver onboard the International Space Station [29]. Thus, risk mitigation considerations suggest the reuse of the Legendre PS method for implementing STMs.

A second, and perhaps more cogent, argument for using the Legendre PS method is that it converges even when other techniques fail [24]. A particular illustration of the confluence of convergence theory and practical implementation is that a method must converge for arbitrary boundary conditions because these points are constantly changing in operational use. In the Legendre PS method, boundary conditions are imposed at the Gauss–Lobatto points and such an implementation is consistent with theory. When boundary conditions are not imposed at the Gauss–Lobatto points, convergence cannot be guaranteed [24]. This immediately eliminates the use of other PS techniques, those for which convergence cannot be ensured, because convergence is an absolute necessity for flight implementation. This aspect is illustrated by the following simple rigid body maneuvering problem due to Gong [25]:

$$(G) \left\{ \begin{array}{l} \text{Minimize} \quad J[\mathbf{x}(\cdot), u(\cdot)] = \int_0^1 v(t)u(t) dt \\ \text{Subject to} \quad \dot{x}(t) = v(t) \\ \quad \dot{v}(t) = -v(t) + u(t) \\ \quad v(t) \geq 0 \\ \quad 0 \leq u(t) \leq 2 \\ \quad (x(0), v(0)) = (0, 1) \\ \quad (x(1), v(1)) = (1, 1) \end{array} \right.$$

In this illustrative problem, a rigid body is required to maneuver from point *A* to point *B* while minimizing the work done. The solution to this problem over a Gauss–Lobatto grid, shown in Fig. 7, indicates that it is indeed flight implementable because the control solution is in agreement with the exact solution when interpolated between the node points. When the same problem is solved over a Gauss–Radau or a Gauss grid, the controls oscillate wildly, as shown in Fig. 8.

Clearly, the only practically implementable solution is the one shown in Fig. 7. What is more alarming about this particular situation

is that the costates for all three grids converge [25,26], leading to a false impression of grid equivalence. Hence, a careful selection of the proper technique is critical to flight implementation. This is why the Legendre PS method was chosen for flight implementation. In particular, the software package DIDO [8] was used for all of the ground computations. The ideal number of Gauss–Lobatto nodes for each maneuver was determined by the spectral algorithm [14] implemented in DIDO. PS theory is discussed in further detail in Ross and Karpenko [24] and additional discussion regarding the proper selection of PS grid is given in Gong et al. [28] and Fahroo and Ross [25–27,38].

C. Preflight Checkout

Preflight checkout was carried out using a series of standard tests that include continuous-time feasibility and discrete-time optimality checks [8,24]. The former are carried out by propagating the optimal control trajectory through the system dynamic equations and the latter are accomplished through the automatic application [4] of the covector mapping principle [24] to verify the necessary conditions on the optimality of each solution. Following the analysis of each maneuver from the computational point of view, the ability of the TRACE spacecraft to properly execute each optimal slew was verified against a high-fidelity simulation model of the spacecraft developed at the Naval Postgraduate School. Similar maneuver verification tests were performed independently by the Flight Operations Team (FOT) at the NASA Goddard Space Flight Center (GSFC) in Greenbelt, Maryland. All of these preflight checkout activities were mandatory because shortest-time maneuvers had not been implemented on any spacecraft prior to our first demonstrations on TRACE [4]. After all of the necessary preflight checkout activities were successfully completed, the authors and the FOT developed the necessary procedures for implementing the maneuvers on orbit.

D. Flight Implementation

A sample ground prediction for the shortest-time maneuver is shown in Fig. 9. The sample maneuver is a 50 deg rotation of the TRACE instrument about the *z*-body axis. The initial and final quaternions for the rest-to-rest slew are $q_0 = [0.1863, 0.0013, 0.0559, 0.9809]^T$ and $q_f = [0.1694, -0.0776, 0.4652, 0.8654]^T$. During the slew, the quaternion histories q_1 and q_2 are seen to be nonmonotonic (Fig. 9a). Hence, the motion of the spacecraft deviates from the eigenaxis. This behavior results from the buildup of the angular rates around all three body axes, as shown in Fig. 9b, and is a consequence of optimal momentum transfer from the reaction wheel array (Fig. 9c). Telemetry results for the flight implementation of the maneuver are shown in Fig. 10.

A comparison of Figs. 9 and 10 shows an excellent agreement between the ground predictions and the flight performance of the spacecraft. Both the traces of the quaternions and the traces of the spacecraft body rates are nearly indistinguishable from one another. Moreover, in contrast to Fig. 6b, the spacecraft body rates did not exceed the imposed limit of 0.5 deg /s during the maneuver. This is because the optimal control solution allows the body rate buildup to

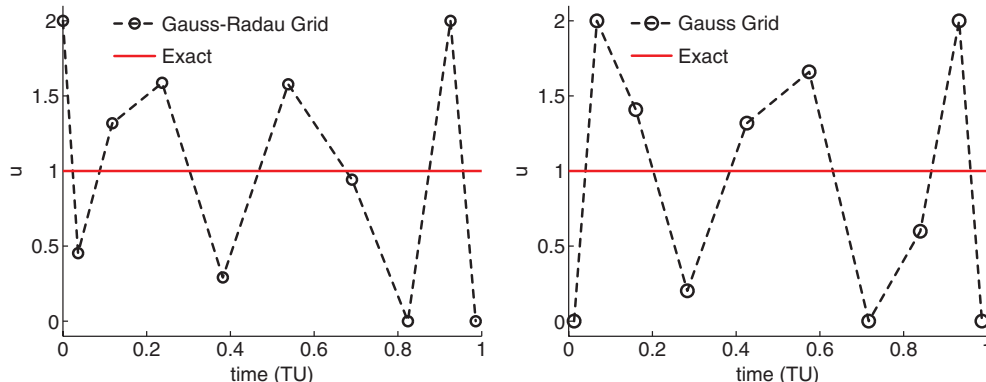
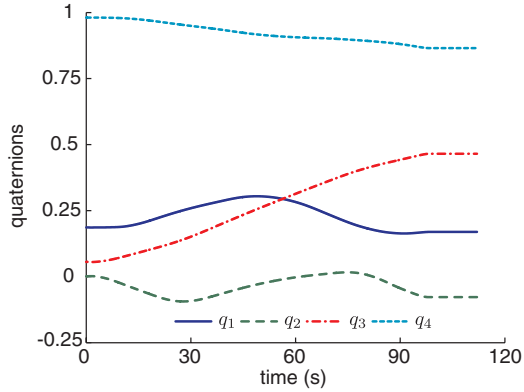
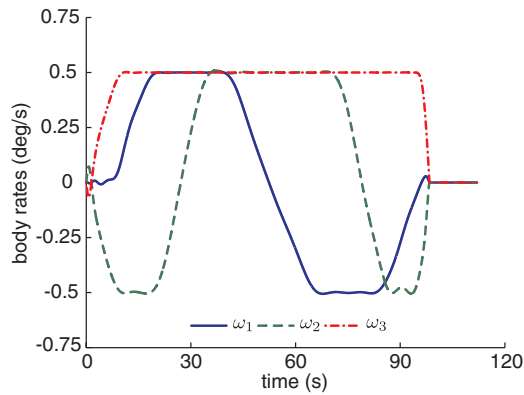


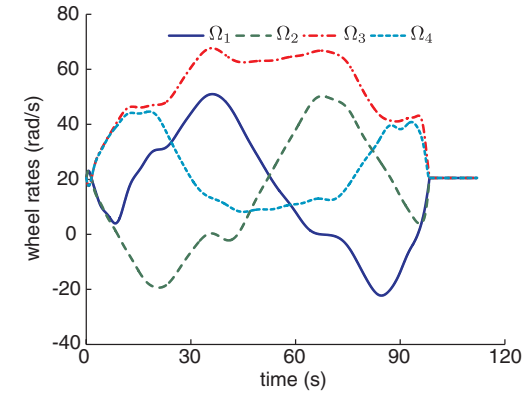
Fig. 8 Non implementable pseudospectral controls: Gauss–Radau grid (left); Gauss grid (right).



a)



b)

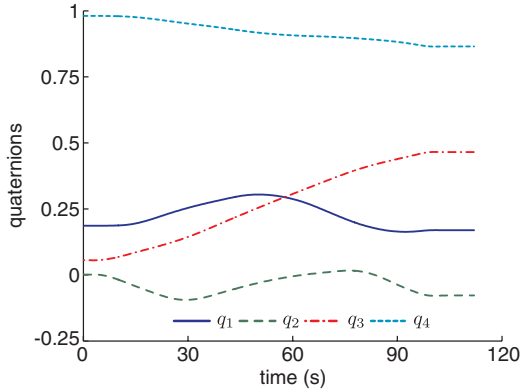


c)

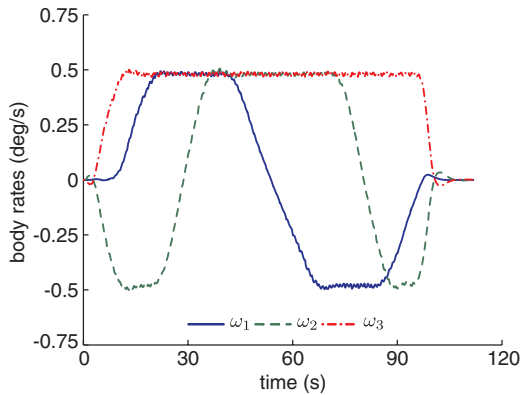
Fig. 9 Ground predictions for a shortest-time reorientation maneuver scheduled to be performed on 19 August 2010: a) quaternions, b) body rates, and c) reaction wheel rates.

be properly controlled throughout the maneuver. The reaction wheel responses obtained from the telemetry data are also in very good agreement with the ground predictions. The small discrepancies in the measured reaction wheel rates can be attributed primarily to uncertainty in the spacecraft inertia tensor and other system parameters.

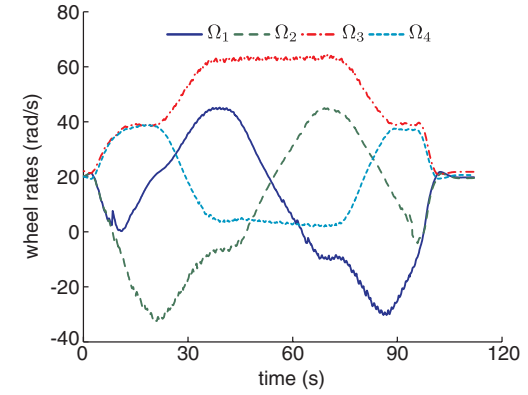
To further illustrate the nature of the spacecraft motion during the maneuver, a three-dimensional visualization was reconstructed from the telemetry data. Figure 11 shows the motion trace of the spacecraft boresight (y -body axis) as the spacecraft rotates through the optimal maneuver. As shown, intermediate rotations about the x and y axes are used in order to maximize the overall maneuver rate. Because the motion trace of the z -body axis is a closed loop that begins and ends at the same point, the flight results show that the intermediate rotations are properly zeroed out in accordance with the specified terminal conditions. Although the telemetry results indicate that it is indeed possible to implement a shortest-time maneuver designed using the



a)



b)



c)

Fig. 10 Flight results for shortest-time reorientation maneuver performed on 19 August 2010: a) quaternions, b) body rates, and c) reaction wheel rates.

proposed process, it is not possible to use this single flight test to generalize how slew performance can be improved over a larger region of operation. This can only be done by real-time implementation over a wide envelope and within the context of maneuvers that are particular to the spacecraft mission. Hence, it is necessary to design, implement, and demonstrate the concepts over several operationally relevant scenarios.

IV. Operationally Relevant Maneuver Demonstrations

This section presents the design and implementation results of several flight demonstrations that were conducted on TRACE in order to illustrate the applicability of shortest-time maneuvering capabilities in scenarios having relevance to imaging operations. In the first demonstration, a multipoint maneuver was designed and executed that minimizes the slew time to image a set of objects. The second flight demonstration shows how optimal maneuvers can be employed to minimize the time to transition between two orthogonal

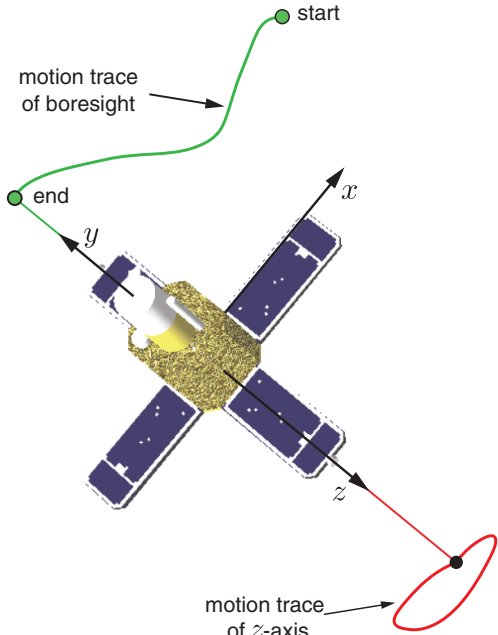


Fig. 11 Visualization of shortest-time reorientation maneuver performed on 19 August 2010 (flight data).

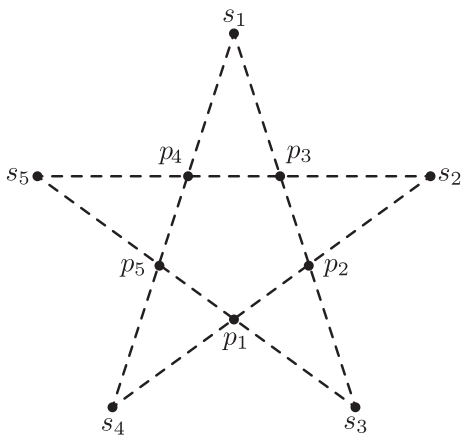


Fig. 12 Emulation of operational environment using a five-pointed star with inscribed pentagon.

imaging swaths. To emulate a realistic operational environment, a five-pointed star configuration was developed (Fig. 12). The five points of the star as well as the five corners of the inscribed pentagon all constitute potential locations for data collection. As shown in Fig. 13, a large angle slew can be constructed by maneuvering between any two extreme points of the star, $s_i \rightarrow s_j$, whereas small angle slews can be constructed by maneuvering between the corners of the pentagon, $p_i \rightarrow p_j$. A mix and match of points between the pentagon and the star can be used to generate medium angle maneuvers, for example $s_i \rightarrow p_j$ or $p_i \rightarrow s_j$. In addition to providing a geometry from which different maneuver sizes can be easily selected, the star configuration also allows maneuvers to be performed along a variety of different eigenaxes so that the spacecraft can be exercised over a larger envelope of operation. This ensures that a good representation of the improvement in maneuvering performance can be obtained from a sample flight test.

A. Multipoint STAR Maneuver

An example of a multipoint maneuver based on the star configuration is given in Table 1. Attitude quaternions as well as the yaw-pitch-roll Euler angles, relative to the final orientation are given. For each point of interest, the nominal rotation about the boresight (pitch) axis is zero. The relevant parameters for performing the

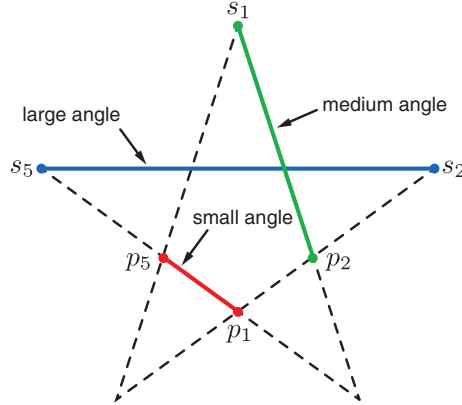


Fig. 13 Illustration of various maneuvers on the five-pointed star.

maneuver sequence as a series of standard slews are given in Table 2. Referring to Table 2, the multipoint STAR maneuver consists of both medium angle (≈ 30 deg) and large angle ($\gg 30$ deg) slews. The objective of the multipoint maneuver experiment is to slew between each desired orientation as quickly as possible while meeting all operational and design constraints.

The multipoint STAR maneuver was executed on board TRACE on 19 August 2010 and monitored at the Multi-Mission Operations Center (MMOC), located at GSFC. As illustrated in Fig. 14, the necessary spacecraft commands were prepared and verified by the FOT using the real-time ITOS system and the TRACE Spacecraft Simulator before being uplinked to the spacecraft. Communication between the MMOC and the spacecraft is done using Near Earth Network of ground stations, namely, the Wallops Ground Network (Wallop Island and McMurdo), Universal Space Network, Alaska Satellite Facility, and Merritt Island Launch Annex. These ground stations provide data acquisition and tracking capabilities in addition to command interfacing. Flight test results obtained from the flight demonstration telemetry are shown in Fig. 15. Figure 15a illustrates the motion of the instrument boresight as a projection on the plane. The traces are reconstructed from telemetry data captured during the maneuver. Figure 15 clearly shows that the motion of the boresight follows differently shaped paths as the spacecraft rotates, in minimum time, between each of the desired collection regions. Time histories of the spacecraft relative Euler angles are shown in Fig. 15b for each maneuver. For comparison, the multipoint STAR maneuver was also performed on TRACE by implementing conventional eigenaxis slews between each of the collection points. The flight test results, given in Fig. 16, show that the boresight traces out the

Table 1 Attitude sequence for multipoint STAR pattern

Orientation	Quaternions				Euler angles, deg		
	q_1	q_2	q_3	q_4	$\Delta\phi$	$\Delta\theta$	$\Delta\psi$
1	0.0602	-0.1850	0.6165	0.7629	-13.5	0.0	23.7
2	0.2860	-0.0069	0.5607	0.7770	18.1	0.0	11.8
3	0.1864	-0.0045	0.0854	0.9788	0.0	0.0	-46.8
4	0.1195	-0.1431	0.7921	0.5812	0.0	0.0	50.8
5	-0.1314	-0.1263	0.2458	0.9520	-37.6	0.0	-24.4
6	0.1693	-0.0781	0.4666	0.8646	0.0	0.0	0.0

Table 2 Eigenaxis maneuver parameters for multipoint STAR pattern

Maneuver	Φ , deg	e_1	e_2	e_3
1 \rightarrow 2	33.7	0.93	-0.01	-0.36
2 \rightarrow 3	61.0	-0.27	-0.15	-0.95
3 \rightarrow 4	97.5	0.0	0.0	1.0
4 \rightarrow 5	82.7	-0.39	0.30	-0.87
5 \rightarrow 6	44.5	0.83	-0.18	0.53

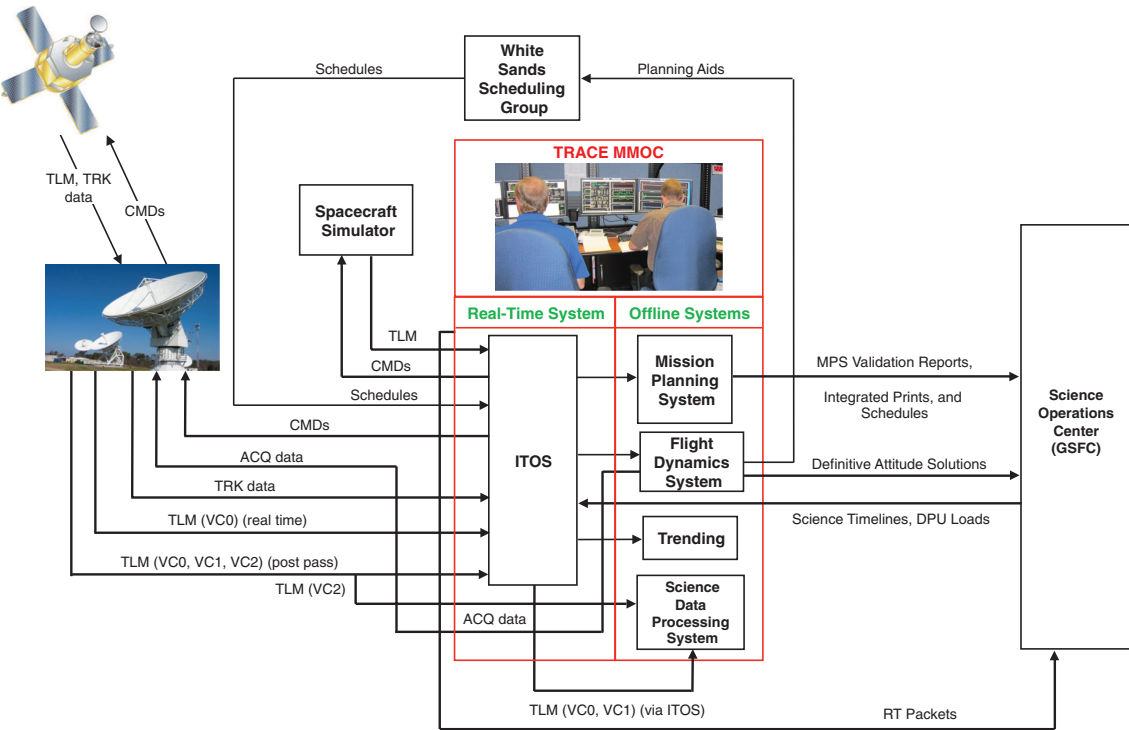
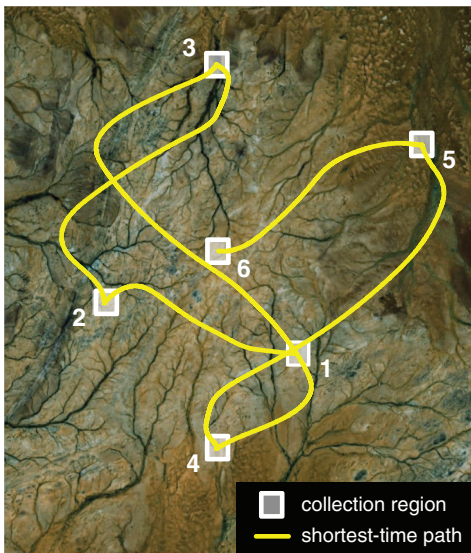
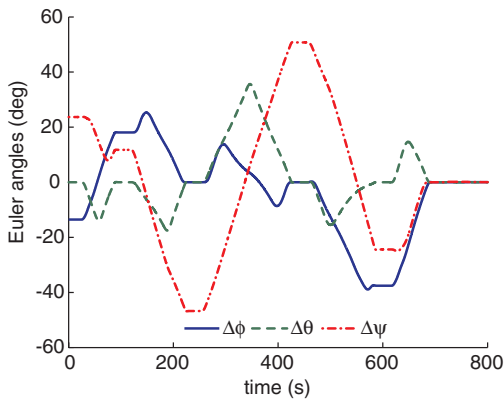


Fig. 14 Schematic of data flow for TRACE mission operations.

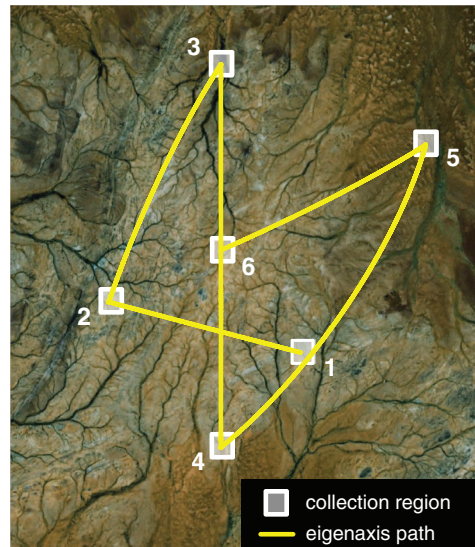


a)

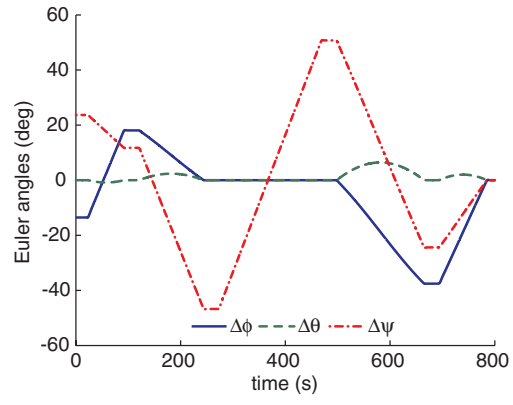


b)

Fig. 15 Flight results for the shortest-time multipoint STAR maneuver performed on 19 August 2010: a) projection of boresight motion, and b) relative yaw-pitch-roll Euler angles.



a)



b)

Fig. 16 Flight results for the conventional multipoint STAR maneuver performed on 20 August 2010: a) projection of boresight motion, and b) relative yaw-pitch-roll Euler angles.

Table 3 Improvement in maneuver performance for multipoint STAR pattern (flight results)

Maneuver	Completion time, s		Performance Improvement	
	Shortest time	Eigenaxis,	Δt , s	Percent
1 → 2	73.2	76.8	3.6	4.7
2 → 3	113.4	130.7	17.3	13.2
3 → 4	180.4	203.8	23.4	11.5
4 → 5	138.3	174.6	36.3	20.8
5 → 6	80.7	98.5	17.8	18.1

expected straight line paths (shortest circular arcs) as the spacecraft rotates between each of the desired orientations. A comparison of Figs. 15b and 16b confirms that the multipoint STAR maneuver can indeed be completed more quickly by allowing the spacecraft to rotate off of the eigenaxis.

Numerical values of the maneuver completion times for the time-optimal and eigenaxis maneuvers are given in Table 3. Table 3 also reports the improvement in maneuver performance that was obtained by using time-optimal maneuvering compared to conventional slews. The flight test results show that the shortest-time slews consistently outperform their eigenaxis counterparts with reductions in maneuver completion times ranging from approximately 5 to 21%. The overall performance improvement across the entire maneuver sequence was about 15%. The exact amount of time savings that is achievable by implementing shortest-time maneuvers is strongly correlated to the particular rigid body configuration under investigation. As such, the improvement in maneuver performance can be much larger than 15% when time-optimal maneuvers are implemented on spacecraft specifically designed for imaging operations. Recent

ground experiments on a CMG-actuated spacecraft simulator at Honeywell have indicated that it is possible to decrease slew times by as much as 50% through the design and implementation of STMs [37]. Thus, the capability of an imaging spacecraft can be substantially improved without any hardware changes.

B. Orthogonal SCAN Maneuver

The orthogonal SCAN maneuver represents another scenario relevant to the operation of an imaging spacecraft. This maneuver emulates an imaging process in which the satellite sensor must collect data along a swath or scan line. The objective in this case is to quickly slew between the transition points that mark the initiation and completion of each scanning operation. In the demonstration, two orthogonal collection swaths, one parallel to and one perpendicular to the assumed ground track, are included to stress the spacecraft attitude control system. This demonstration illustrates how optimal maneuvers can be used to quickly transition a spacecraft between point collection and scanning operations, each of which may have requirements for different, nonzero, terminal rates.

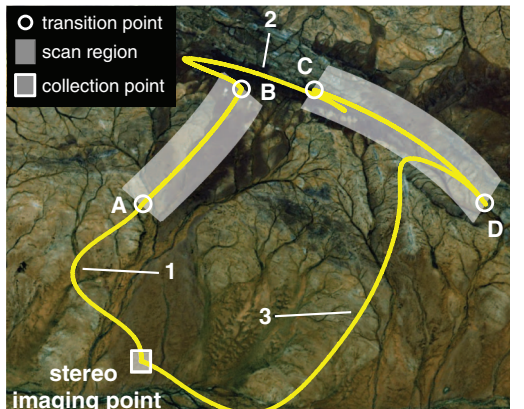
Telemetry results for the SCAN maneuver test are shown in Fig. 17. Figure 17a shows the motion trace of the imaging boresight. Referring to Fig. 17a, the first maneuver starts from a point collection region and ends when the spacecraft reaches the attitude and rate conditions specified at location A. Once reaching transition point A, nonzero attitude rates are maintained in order to perform the scanning operation (Fig. 17b). To transition from the first scan region to the second scan region, which lies in a direction orthogonal to the first, a second maneuver is performed between points B and C. Once the desired spacecraft attitude and rates are reached at point C, a second scan operation is performed by maintaining the specified nonzero body rates between attitudes C and D. The SCAN scenario is completed by a final maneuver between transition point D and the initial point collection region. Returning to the initial position emulates an opportunity for stereo imaging. A particularly interesting feature of the SCAN maneuver is the path traced out by the spacecraft boresight as the vehicle transitions between the two orthogonal scan regions. In particular, the spacecraft first moves away from and then overshoots point C before initiating the second scan. This surprising and unexpected result emphasizes how the optimal control approach for spacecraft maneuver design challenges intuition and can thus be leveraged to enhance the capability of an imaging spacecraft.

V. Conclusions

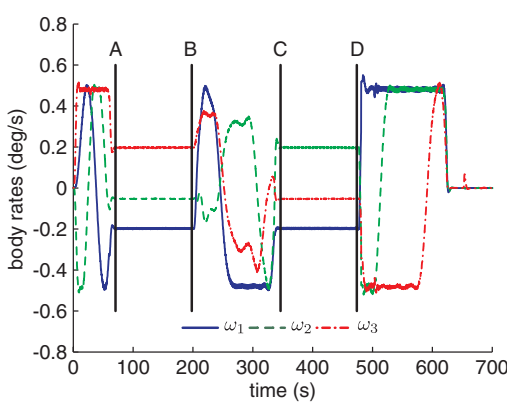
The series of successful flight demonstrations of operationally relevant slew maneuvers illustrated how the proposed maneuver design process can be used to more efficiently transition a spacecraft between point collection, scanning, tracking, and other operational tasks routinely carried out by imaging satellites. Thus, it is now possible to apply the approach to other, nonimaging, spacecraft that might benefit from increased slew performance. Favorable conditions for this advancement were made possible by a combination of optimal control theory and pseudospectral theory at their most fundamental levels. This joint concept, known as pseudospectral optimal control theory (a term coined by Ross) was the key to successful flight implementation of the maneuvers and their current transition to operational use. As a result of this advancement, there are now new opportunities for research in science, engineering, and operations. For instance, the collection of multipoint optimal control problems that was posed and solved in this paper can be inserted into the larger framework of hybrid optimal control wherein the collection planning problem is jointly optimized to maximize data collection.

Acknowledgments

The authors wish to acknowledge K. Lebsack (NASA Engineering and Safety Center), R. Chen (K & D Research), and T. Correll of the NASA Goddard Space Flight Center (GSFC) for their help in explaining the intricacies of the TRACE spacecraft and its attitude control system as well as the tireless assistance of O. Cuevas (GSFC).



a)



b)

Fig. 17 Flight results for the orthogonal SCAN maneuver performed on 27 August 2010: a) projection of boresight motion, and b) spacecraft body rates.

M. Baugh (GSFC), S. Snell (Computer Sciences Corporation), D. Bradley (Honeywell Technology Solutions), and the outstanding efforts of the flight operations team in the Multi-Mission Operations Center at the GSFC who were instrumental in coordinating the flight experiments. The authors also thank NASA for recognizing this work with the NASA Group Achievement Award.

References

- [1] Cordeau, J.-F., and Laporte, G., "Maximizing the Value of an Earth Observation Satellite Orbit," *Journal of the Operational Research Society*, Vol. 56, No. 6, 2005, pp. 962–968.
doi:10.1057/palgrave.jors.2601926
- [2] Mansour, M. A. A., and Dessouky, M. M., "A Genetic Algorithm Approach for Solving the Daily Photography Selection Problem of the SPOT5 Satellite," *Computers and Industrial Engineering*, Vol. 58, No. 3, 2010, pp. 509–520.
doi:10.1016/j.cie.2009.11.012
- [3] Scrivener, S. L., and Thompson, R. C., "Survey of Time-Optimal Attitude Maneuvers," *Journal of Guidance, Control, and Dynamics*, Vol. 17, No. 2, 1994, pp. 225–233.
doi:10.2514/3.21187
- [4] Karpenko, M., Bhatt, S., Bedrossian, N., Fleming, A., and Ross, I. M., "First Flight Results on Time-Optimal Spacecraft Slews," *Journal of Guidance, Control, and Dynamics*, Vol. 35, No. 2, 2012, pp. 367–376.
doi:10.2514/1.54937
- [5] Bilitoria, K. D., and Wie, B., "Time-Optimal Three-Axis Reorientation of Rigid Spacecraft," *Journal of Guidance, Control, and Dynamics*, Vol. 16, No. 3, 1993, pp. 446–452.
doi:10.2514/3.21030
- [6] Shen, H., and Tsiotras, P., "Time-Optimal Control of Axisymmetric Rigid Spacecraft Using Two Controls," *Journal of Guidance, Control, and Dynamics*, Vol. 22, No. 5, 1999, pp. 682–694.
doi:10.2514/2.4436
- [7] Proulx, R., and Ross, I. M., "Time-Optimal Reorientation of Asymmetric Rigid Bodies," *Advances in the Astronautical Sciences*, Vol. 109, 2001, pp. 1207–1227.
- [8] Ross, I. M., "A Beginner's Guide to DIDO: A MATLAB Application Package for Solving Optimal Control Problems," Elissar Global, Rept. TR-711, Carmel, CA, Nov. 2007.
- [9] Fleming, A., "Real-Time Optimal Slew Maneuver Design and Control," Engineer's Thesis, Mechanical and Aerospace Engineering Dept., Naval Postgraduate School, Monterey, CA, Dec. 2004.
- [10] Fleming, A., Sekhavat, P., and Ross, I. M., "Minimum-Time Reorientation of a Rigid Body," *Journal of Guidance, Control, and Dynamics*, Vol. 33, No. 1, 2010, pp. 160–170.
doi:10.2514/1.43549
- [11] Fleming, A., and Ross, I. M., "Singularity-Free Optimal Steering of Control Moment Gyros," *Advances in the Astronautical Sciences*, Vol. 123, 2006, pp. 2681–2700.
- [12] Fleming, A., and Ross, I. M., "Optimal Control of Spinning Axisymmetric Spacecraft: A Pseudospectral Approach," *AIAA Guidance, Navigation, and Control Conference*, AIAA Paper 2008-7164, 2008.
- [13] Fleming, A., Sekhavat, P., and Ross, I. M., "Constrained, Minimum-Time Maneuvers for CMG Actuated Spacecraft," *Advances in the Astronautical Sciences*, Vol. 135, 2009, pp. 1009–1028.
- [14] Gong, Q., Fahroo, F., and Ross, I. M., "A Spectral Algorithm for Pseudospectral Methods in Optimal Control," *Journal of Guidance, Control, and Dynamics*, Vol. 31, No. 3, 2008, pp. 460–471.
doi:10.2514/1.32908
- [15] Ross, I. M., and Fahroo, F., "Pseudospectral Knotting Methods for Solving Optimal Control Problems," *Journal of Guidance, Control, and Dynamics*, Vol. 27, No. 3, 2004, pp. 397–405.
doi:10.2514/1.3426
- [16] Kang, W., Gong, Q., and Ross, I. M., "On the Convergence of Nonlinear Optimal Control Using Pseudospectral Methods for Feedback Linearizable Systems," *International Journal of Robust and Nonlinear Control*, Vol. 17, No. 14, 2007, pp. 1251–1277.
doi:10.1002/(ISSN)1099-1239
- [17] Kang, W., Ross, I. M., and Gong, Q., "Pseudospectral Optimal Control and its Convergence Theorems," *Analysis and Design of Nonlinear Control Systems*, Springer-Verlag, Berlin, 2008, pp. 109–126.
- [18] Kang, W., "Rate of Convergence for the Legendre Pseudospectral Optimal Control of Feedback Linearizable Systems," *Journal of Control Theory and Applications*, Vol. 8, No. 4, 2010, pp. 391–405.
doi:10.1007/s11768-010-9104-0
- [19] Ross, I. M., Sekhavat, P., Fleming, A., and Gong, Q., "Optimal Feedback Control: Foundations, Examples and Experimental Results for a New Approach," *Journal of Guidance, Control, and Dynamics*, Vol. 31, No. 2, 2008, pp. 307–321.
doi:10.2514/1.29532
- [20] Karpenko, M., Bhatt, S., Bedrossian, N., and Ross, I. M., "Design and Flight Implementation of Operationally Relevant Time-Optimal Spacecraft Maneuvers," *AAS/AIAA Astrodynamics Specialist Conference*, AAS Paper 2011-586, 2011.
- [21] Karpenko, M., Bhatt, S., Bedrossian, N., and Ross, I. M., "Flight Results for a Revolutionary Approach to Maximizing Spacecraft Imaging Capability," *International Symposium on Space Flight Dynamics*, NASA Jet Propulsion Laboratory, 2012, http://issfd.org/ISSFD_2012/ISSFD23_AD_2.pdf [retrieved 22 Mar. 2013].
- [22] Ross, I. M., and D'Souza, C. D., "Hybrid Optimal Control Framework for Mission Planning," *Journal of Guidance, Control, and Dynamics*, Vol. 28, No. 4, 2005, pp. 686–697.
doi:10.2514/1.8285
- [23] Ross, I. M., and Fahroo, F., "Discrete Verification of Necessary Conditions for Switched Nonlinear Optimal Control Systems," *American Control Conference*, IEEE, Piscataway, NJ, Vol. 2, 2004, pp. 1610–1615.
- [24] Ross, I. M., and Karpenko, M., "A Review of Pseudospectral Optimal Control: From Theory to Flight," *Annual Reviews in Control*, Vol. 36, No. 2, 2012, pp. 182–197.
doi:10.1016/j.arcontrol.2012.09.002
- [25] Fahroo, F., and Ross, I. M., "Convergence of the Costates Does Not Imply Convergence of the Control," *Journal of Guidance, Control, and Dynamics*, Vol. 31, No. 5, 2008, pp. 1492–1497.
doi:10.2514/1.37331
- [26] Fahroo, F., and Ross, I. M., "Advances in Pseudospectral Methods for Optimal Control," *AIAA Guidance, Navigation, and Control Conference*, AIAA Paper 2008-7309, 2008.
- [27] Fahroo, F., and Ross, I. M., "Enhancing the Practical Agility of UAVs via Pseudospectral Optimal Control," *Lecture Notes in Control and Information Sciences: Recent Advances in Research on Unmanned Aerial Vehicles*, Vol. 444, Springer-Verlag, New York, 2013, pp. 1–30.
- [28] Gong, Q., Ross, I. M., and Fahroo, F., "Pseudospectral Optimal Control on Arbitrary Grids," *Advances in the Astronautical Sciences*, Vol. 135, 2009, pp. 1741–1760.
- [29] Kang, W., and Bedrossian, N., "Pseudospectral Optimal Control Theory Makes Debut Flight, Saves NASA \$1M in Under 3 Hrs," *SIAM News*, Vol. 40, No. 7, Sept. 2007, p. 1.
- [30] Bedrossian, N., Karpenko, M., and Bhatt, S., "Overclock My Satellite: Sophisticated Algorithms Boost Satellite Performance on the Cheap," *IEEE Spectrum*, Vol. 49, No. 11, 2012, pp. 54–62.
doi:10.1109/MSPEC.2012.6341207
- [31] Zimbelman, D., Wilmot, J., and Evangelista, S., "The Attitude Control System Design for the Transition Region and Coronal Explorer Mission," *Proceedings of the 10th Annual AIAA/USU Conference on Small Satellites*, Center for Space Engineering, Utah State Univ., Logan, UT, 1996, pp. 1–7.
- [32] Schaub, H., and Junkins, J. L., *Analytical Mechanics of Space Systems*, AIAA, Reston, VA, 2003, pp. 11–13.
- [33] Sidi, M. J., *Spacecraft Dynamics and Control*, Cambridge Univ. Press, New York, 1997, pp. 104–105.
- [34] Ross, I. M., *A Primer on Pontryagin's Principle in Optimal Control*, Collegiate Publishers, San Francisco, 2009, pp. 37–38.
- [35] Bedrossian, N., Bhatt, S., Lammers, M., and Nguyen, L., "Zero Propellant Maneuver: Flight Results for 180° ISS Rotation," *International Symposium on Space Flight Dynamics*, NASA Goddard Space Flight Center, 2007, http://issfd.org/ISSFD_2007/15-4.pdf [retrieved 22 Mar. 2013].
- [36] Bedrossian, N., Bhatt, S., Kang, W., and Ross, I. M., "Zero-Propellant Maneuver Guidance," *IEEE Control Systems Magazine*, Vol. 29, No. 5, 2009, pp. 53–73.
doi:10.1109/MCS.2009.934089
- [37] Karpenko, M., Bhatt, S., and Hamilton, B., "Application of Pseudospectral Optimal Control for Shortest-Time Spacecraft Attitude Maneuvers," *IEEE Conference on Decision and Control: Workshop on Guidance, Navigation and Control Applications in the Aerospace Industry*, IEEE Technical Committee on Aerospace Controls, 2012.
- [38] Fahroo, F., and Ross, I. M., "Pseudospectral Methods for Infinite Horizon Nonlinear Optimal Control Problems," *Journal of Guidance, Control, and Dynamics*, Vol. 31, No. 4, 2008, pp. 927–936.
doi:10.2514/1.33117